Accepted for publication in *The Astrophysical Journal*
Preprint typeset using LaTeX style emulateapj v. 10/09/06

THE *SPITZER* SURVEY OF THE SMALL MAGELLANIC CLOUD: DISCOVERY OF EMBEDDED PROTOSTARS IN THE H II REGION NGC 346

Joshua D. Simon[1], Alberto D. Bolatto[2], Barbara A. Whitney[3], Thomas P. Robitaille[4], Ronak Y. Shah[5], David Makovoz[6], Snežana Stanimirović[7], Rodolfo H. Barbá[8], and Mónica Rubio[9]

Accepted for publication in The Astrophysical Journal

ABSTRACT

We use *Spitzer Space Telescope* observations from the *Spitzer* Survey of the Small Magellanic Cloud (S^{3}MC) to study the young stellar content of N66, the largest and brightest H II region in the SMC. In addition to large numbers of normal stars, we detect a significant population of bright, red infrared sources that we identify as likely to be young stellar objects (YSOs). We use spectral energy distribution (SED) fits to classify objects as ordinary (main sequence or red giant) stars, asymptotic giant branch stars, background galaxies, and YSOs. This represents the first large-scale attempt at blind source classification based on *Spitzer* SEDs in another galaxy. We firmly identify at least 61 YSOs, with another 50 probable YSOs; only one embedded protostar in the SMC was reported in the literature prior to the S^{3}MC. We present color selection criteria that can be used to identify a relatively clean sample of YSOs with IRAC photometry. Our fitted SEDs indicate that the infrared-bright YSOs in N66 have stellar masses ranging from 2 $M_\odot$ to 17 $M_\odot$, and that approximately half of the objects are Stage II protostars, with the remaining YSOs roughly evenly divided between Stage I and Stage III sources. We find evidence for primordial mass segregation in the H II region, with the most massive YSOs being preferentially closer to the center than lower-mass objects. Despite the low metallicity and dust content of the SMC, the observable properties of the YSOs appear consistent with those in the Milky Way. Although the YSOs are heavily concentrated within the optically bright central region of N66, there is ongoing star formation throughout the complex and we place a lower limit on the star formation rate of 3.2×10^{-3} $M_\odot$ yr^{-1} over the last $\sim$1 Myr.

Subject headings: Magellanic Clouds — H II regions — infrared: stars — ISM: individual (N66) — stars: formation — stars: pre-main sequence

1. INTRODUCTION

Star formation is one of the most important astrophysical processes, but because it takes place on small physical scales and behind heavy optical obscuration, observations of the early phases of star formation have generally been limited to the Milky Way. Only in recent years have these studies begun to be extended to extragalactic objects. Now, the high sensitivity, high angular resolution, and large field of view provided by the *Spitzer Space Telescope* at mid-infrared wavelengths open a new window on recently formed stars in nearby galaxies like the Magellanic Clouds. Studying these young stellar objects (YSOs) provides an excellent complement to observations of star formation in the Milky Way because the physical conditions they are subject to are quite different from those in the Galaxy. In particular, the metallicity of the Magellanic Clouds is well below solar, and their dust content is correspondingly lower as well (Stanimirović et al. 2000; Leroy et al. 2007). Most star formation today is taking place in galaxies smaller than the Milky Way (for which the Magellanic Clouds are good prototypes), and star formation at high redshift occurred in low-metallicity environments, so investigating the effects of these differences on how star formation works will be an important step towards understanding how many of the stars in the universe were formed.

The Small Magellanic Cloud (SMC), and its more massive companion the Large Magellanic Cloud (LMC), are the two nearest star-forming dwarf galaxies. Located at a distance of 61.1 kpc (Westerlund 1997; Storm et al. 2004; Hilditch, Howarth, & Harries 2005; Keller & Wood 2006), and with a luminosity of $\sim 6 \times 10^8$ $L_\odot$ (de Vaucouleurs et al. 1991) and a metallicity of $\sim$ 1/5 solar (Dufour 1975; Peimbert & Torres-Peimbert 1976; Dufour & Harlow 1977; Peimbert, Peimbert, & Ruiz 2000), the SMC is perhaps the best local analog of primitive galaxies. The SMC is actively forming stars at a rate of ~ 0.05 $M_\odot$ yr^{-1} (Wilke et al. 2004), and is populated by well studied H II regions and young star clusters. The most active star-forming region is NGC 346 (alternately known as N66; Henize 1956), located toward the northern end of the SMC bar. The OB association powering N66 contains 33

[1] Department of Astronomy, California Institute of Technology, 1200 E. California Blvd, MS 105-24, Pasadena, CA 91125; jsimon@astro.caltech.edu
[2] Department of Astronomy, University of California at Berkeley, 601 Campbell Hall, Berkeley, CA 94720; bolatto@astro.berkeley.edu
[3] Space Science Institute, 4750 Walnut Street, Suite 205, Boulder, CO 80301; bwhitney@spacescience.org
[4] SUPA, School of Physics and Astronomy, University of St. Andrews, North Haugh, St. Andrews, KY16 9SS, UK; tr9@st-andrews.ac.uk
[5] Institute for Astrophysical Research, Boston University, 725 Commonwealth Avenue, Boston, MA 02215; ronak@bu.edu
[6] *Spitzer* Science Center, California Institute of Technology, 1200 E. California Blvd., MS 220-6, Pasadena, CA 91125; davidm@ipac.caltech.edu
[7] Department of Astronomy, University of Wisconsin, 475 North Charter Street, Madison, WI 53706; sstanimi@astro.wisc.edu
[8] Departamento de Física, Universidad de La Serena, Benavente 980, La Serena, Chile; rbarba@xeneize.dfuls.cl
[9] Departamento de Astronomía, Universidad de Chile, Casilla 36-D, Santiago, Chile; monica@das.uchile.cl

spectroscopically confirmed O stars, and a similar number of bright blue stars without spectra that are likely to be O stars as well (Massey, Parker, & Garmany 1989)

In this paper, we employ *Spitzer* observations from the *Spitzer* Survey of the Small Magellanic Cloud (S^{3}MC; Bolatto et al. 2007, hereafter B07) to locate objects in N66 with mid-infrared excesses that we identify as candidate YSOs. In the following section, we very briefly describe the observations and our photometry. In §3, we classify the detected sources by fitting their spectral energy distributions and study their locations in color-color space. In §4 we discuss some of the implications of our results and compare to recent optical studies of N66. We summarize our findings in §5.

2. OBSERVATIONS, DATA REDUCTION, AND ANALYSIS

The S^{3}MC is a project to map the star-forming body of the SMC with *Spitzer* in all seven Infrared Array Camera (IRAC; Fazio et al. 2004) and Multiband Imaging Photometer for *Spitzer* (MIPS; Rieke et al. 2004) bands. The images cover an area of ~ 3 deg^2 including the entire bar and wing of the SMC, with an average exposure time of 144 s at each position. The MIPS data were obtained in 2004 November and the IRAC data in 2005 May. The data were processed with version S11.4 of the automated *Spitzer* pipeline. We constructed mosaic images from the individual Basic Calibrated Data frames using the Mosaicking and Point Source Extraction (MOPEX) software provided by the *Spitzer* Science Center (SSC). B07 describe further details of the observations and the data processing.

We performed photometry on the mosaic images with the Astronomical Point Source Extraction (APEX) tasks in the MOPEX package (Makovoz & Marleau 2005). We selected a set of $20-30$ bright stars in each band that were as isolated as possible and constructed point response functions (PRFs) directly from the data. We then fit these PRFs to every detected source in the images to determine fluxes. The images contain extensive diffuse emission that must be separated from point sources, so we used a small median filter ($8\farcs4$) to remove the background, and then detected sources on the background-subtracted image. Because the median filtering removes some flux even from point sources, the PSF fitting then took place on the original (not background subtracted) image. We found that this technique offered the best compromise between detecting bright sources on top of diffuse emission and detecting faint sources in background-free regions. For the 24 μm MIPS data, in which the extended emission dominates over the point sources, we used a somewhat larger median filter ($27\farcs5$) and switched to the 'combo' algorithm for separating clusters of bright emission into individual sources in place of the 'peak' algorithm in the task DETECT.[10] We used observations of bright, isolated point sources in the SMC to measure the aperture corrections for the photometry. To provide near-infrared fluxes, we used VLT/ISAAC J and K_s imaging of the center of N66 (Rubio et al. 2002, Rubio & Barbá, in preparation) and Two Micron All Sky Survey (2MASS; Skrutskie et al. 2006) measurements in the outer regions. We also added *HST* V- and I-band photometry of the central region from Gouliermis et al. (2006), but because the much higher angular resolution of the ACS images can cause confusion within the *Spitzer* resolution element, we only used these data for bright stars ($V \leq 17.5$).

The assumed photometric uncertainty associated with each flux measurement is very important for determining the relative weights given to the various data points in the SED fitting that we carry out in §3.2. Although the statistical uncertainties on all of the photometric measurements were quite small (generally a few percent or less), we imposed larger minimum uncertainties on all of the data points to account for systematics. For example, the *HST*, 2MASS, VLT, IRAC, and MIPS observations were made at various times over a period of 7 years, providing plenty of time for the fluxes of the YSOs, which may be variable, to change. The absolute photometric accuracy of IRAC is 10% (Fazio et al. 2004), so we added 10% of the flux in quadrature to the measured uncertainty for each source. MIPS also has a stated accuracy of 10% (Rieke et al. 2004), so when combined with the IRAC calibration accuracy and the 6 month time baseline between the observations, we used a 20% minimum error for MIPS fluxes. Since the near-IR observations took place $6-7$ years earlier, we imposed larger minimum errors of 35% (for the deep VLT data) and 50% (for the shallow 2MASS data) on those data points. The optical measurements are more recent (2004 July) and more accurate, so we assumed 10% uncertainties on the *HST* photometry.

3. RESULTS

3.1. *Photometry*

For the purposes of this study, we limited our point-source fitting to a $12\farcm75 \times 12\farcm75$ region covering the full extent of the hot dust emission from N66 seen in our 24 μm image (from $00^h57^m51^s$ to $01^h00^m37^s$ and from $-72°16'48''$ to $-72°04'19''$ [all coordinates J2000.0]). In this box, we detect 6544 sources at 3.6 μm, 5836 at 4.5 μm, 1784 at 5.8 μm, 1718 at 8.0 μm, 101 at 24 μm, and 15 at 70 μm, for a total of 8011 unique objects. A significant number of these objects have *Spitzer* colors that are redder than normal stars should be at these wavelengths, suggesting that they may be YSOs or background galaxies (B07).

3.2. *SED Fitting*

There are two possible approaches to determining the nature of individual *Spitzer* sources. One could simply use the observed colors and magnitudes to classify the sources into various categories. Stars of nearly all kinds (except those with dusty atmospheres) have colors near zero for any combination of *Spitzer* bands because the IRAC and MIPS bands are on the Rayleigh-Jeans tail of their spectral energy distributions (SEDs).[11] YSOs, because of the emission from warm ($T \sim 200$ K) dust around the central protostar, have red colors throughout the mid-IR. IRAC colors for theoretical YSO models

[10] More information about the DETECT task and its associated options can be found in the documents titled *APEX User's Guide* and *Image Segmentation* (both by D. Makovoz) that are available on the *Spitzer Science Center* website.

[11] Note that we use the Vega magnitude system throughout this paper.

are given by, e.g., Allen et al. (2004) and Whitney et al. (2003a,b, 2004). Alternatively, one can compare the full SEDs to a variety of source models and find the best match for each object.

The advantage of the color selection strategy is its simplicity, but it also has some drawbacks. It fails to use all of the available information about each object (since we also have MIPS, optical, and near-IR fluxes for many of the sources), and it is very difficult to learn about the detailed properties of individual sources from only their colors. Color selection also does not offer a way to test the assumption that SED models designed for Milky Way sources offer a good description of YSOs that form in the metal- and dust-poor environment of the SMC; this is a disadvantage for studies seeking to determine how star formation proceeds at low metallicity, but could also be an advantage in that it enables the selection of YSOs without regard to the properties of their environment. Because the SED classification should be more accurate, we begin with that technique and then compare the results to color selection in §3.3.

The SED fitting tool used for this study employs a linear regression method to find all the SEDs from a large grid of models that fit the data within a specified χ^2 (Robitaille et al. 2007). The grid of models consists of 7853 stellar atmospheres (Kurucz 1992; Brott & Hauschildt 2005) encompassing all available metallicities and effective temperatures, a limited number of *Infrared Space Observatory* (ISO) spectra of galaxies (Dale et al. 2005; Silva et al. 1998) and AGB stars (Sylvester et al. 1999; Olivier et al. 2001; Hony 2002; Molster et al. 2002; Hony et al. 2002; Fujii & Nakada 2003), and the 20,000 YSO models from Robitaille et al. (2006) computed using the radiation transfer codes from Whitney et al. (2003a,b, 2004). Each YSO model outputs SEDs for 10 viewing angles, so the YSO grid effectively contains 2×10^5 SEDs. The foreground extinction, A_V, is fit simultaneously using an extinction law derived from GLIMPSE observations (Indebetouw et al. 2006). At ultraviolet and visible wavelengths, this extinction law is not appropriate for the SMC, but in the near-IR and mid-IR the differences in extinction between the SMC and Galaxy are small (Gordon et al. 2003; Cartledge et al. 2005). The fitter is run first using only the stellar atmosphere grid. It is then run three more times using the YSO grid, ISO galaxy spectra, and ISO AGB spectra on the sources that are not well-fit by stellar atmospheres. Based on all the successful fit results, defined by their χ^2 values (see below), we can classify sources and calculate best estimates and uncertainties for each model parameter.

We fit an SED for every object for which we had at least four flux measurements. To better constrain the fits at long wavelengths where most of the sources were not detected, we added 24 μm upper limits of 1 mJy (5 times the limiting sensitivity of the 24 μm data) for each source that was not detected at 24 μm. Because there are many more model parameters than data points that go into each observed SED, the traditional reduced χ^2 statistic cannot be used to evaluate the success of the fits. As a proxy, we calculate the χ^2 per data point (where each SED has between 4 and 11 data points). Given this definition, it is difficult to establish *a priori* the division between good and poor fits. We inspected the fits by eye and determined that fits with a χ^2 per data point of less than 2.2 could reasonably be interpreted as good fits, while higher χ^2 values indicated fits that were not a good match to the templates. We will therefore use this cutoff point to separate good and poor fits throughout the paper. Note that this definition depends on the flux uncertainties imposed in §2.

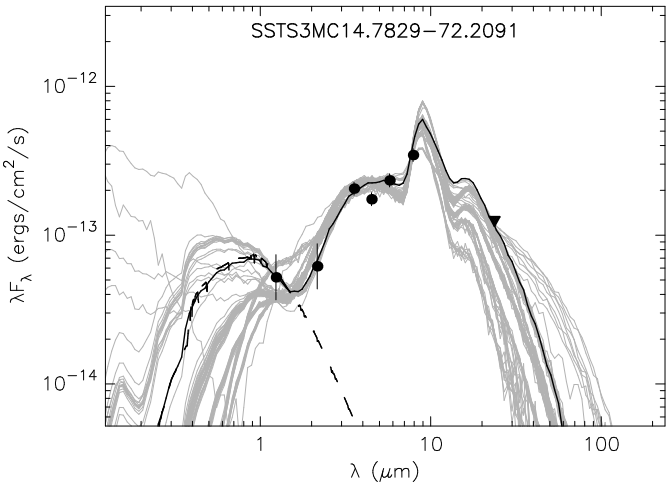

FIG. 1.— Sample SED fits for a YSO in N66. The black points indicate the measured fluxes and uncertainties, and the black triangles are for upper limits. The thin black line represents the best fitting SED, and the gray lines represent all other acceptable (χ^2/data point $\leq$ 2.2) YSO fits. The dashed line represents the stellar photosphere model (including the effect of foreground extinction). This object is a Stage II YSO with a stellar mass of 4.9 $M_\odot$ (see §3.4 for the definition of YSO stages).

3.2.1. *Results From Successful SED Fits*

Out of the 1645 sources with four or more fluxes, 1322 (80.4%) are succesfully fit with stellar SEDs (see above for what we mean by a "successful fit"). Of the remaining 323 sources, 61 can only be fit successfully by YSO models, 27 are background galaxies, 6 are AGB stars, 81 can be fit by multiple classes of models, and 148 cannot be fit by any of the available templates. We display one example YSO SED in Figure 1.

For the sources that can be well-described by multiple types of templates, we used the χ^2 value of the best fit for each template type to attempt a more accurate classification. We set a cutoff of 1.5 times the best χ^2 value, and if, for example, the best YSO fit had $\chi^2 = 1.0$ and the best galaxy fit had $\chi^2 = 1.6$ then we classified the object as a probable YSO. This choice of a χ^2 cutoff indeed results in the majority of the uncertain objects being classified as YSOs and leaves very few objects with unknown types, which appears to be a reasonable outcome. While the exact value chosen for the cutoff is arbitrary, it is clear from the spatial distribution of the various object types that many of the sources classified as possible or definite galaxies must actually be YSOs. The results of this paper do not depend strongly on the exact value of the cutoff. Using this method, we were able to obtain probable classifications for 68 of the 81 objects of uncertain type, including 50 YSOs, 13 galaxies, and 5 AGB stars. Thus, the final object counts are 111 YSOs, 40 galaxies, and 11 AGB stars. The remaining 13 objects had χ^2 values for multiple object types that were too close to distinguish reliably. We list selected parameters from

the fits for all 111 YSOs in Table 1, and we summarize the source classification results in Table 1.

3.2.2. *Objects Poorly Fit by the SED Models*

We inspected each of the 148 poorly fit sources and the various attempted fits to their SEDs to determine why the fitting failed for them. We found that slightly more than 1/3 of the objects had SEDs at short wavelengths that appeared stellar in origin, but the long wavelength data (often at 24 μm) were significantly in excess of the extrapolated photospheric emission. The fits to these sources appear to have failed for a number of reasons including slight mismatches between the optical and IR photometry (either from variability or measurement error), confusion, misidentification of the long wavelength counterparts, and contamination of the photometry by underlying dust emission (revealed by PAH features). However, some of these sources may also have true infrared excesses indicating the presence of circumstellar material. Another $\sim$ 1/3 of the bad fits were generally faint sources that are spatially coincident with dust filaments in the *Spitzer* images, again causing significant contamination of their SEDs by PAH features in the IRAC bands. Some of these objects are probably point sources (either stars or YSOs), while others may simply be unresolved dust knots. The final 1/3 of the bad fits was a mixed population whose SEDs could not be straightforwardly interpreted. Photometric errors in one or more bands and blending were likely responsible for the failure to fit these objects, but they represented only 2.6% of the total sample.

3.3. *IRAC Colors of YSOs*

Using the results of the SED fitting, we can now investigate the colors of the objects classified as YSOs and as stars. We display four color-color plots in Figure 2 to illustrate the possibilities for color selection. Stars, as expected, lie in the cloud of points centered near (0, 0), while sources that are red in one or both colors may be YSOs. Note that the frequently used [3.6]−[4.5] vs. [5.8]−[8.0] color-color plot (Fig. 2a) does not cleanly separate YSOs from other types of sources, particularly stars with modest IR excesses and sources with PAH contamination. Better separation can be achieved using different combinations of colors, as shown in Figure 2b. These plots take advantage of longer color baselines and the abrupt change in YSO spectra between the 4.5 μm and 5.8 μm bands to distinguish YSOs from stars, galaxies, and PAHs. These results demonstrate that while color selection can be a useful technique for identifying YSOs, it does not appear possible to obtain a YSO sample that is both complete and clean with a simple set of color diagnostics. SED fitting is a more comprehensive way to determine the nature of sources if measurements in enough bands are available. Nevertheless, because in many cases it is desirable to classify objects with easily applicable techniques, we use our data to provide guidance for color selection of YSOs.

Assuming that the purple points in Figure 2 are indeed YSOs, one can select YSOs with the following set of criteria:

$$
\begin{aligned}
&[3.6]-[4.5] > 0.6\times([4.5]-[8.0])-1.0\\
&[4.5]-[8.0] < 2.8\\
&[3.6]-[4.5] < 0.6\times([4.5]-[8.0])+0.3\\
&[3.6]-[4.5] > -([4.5]-[8.0])+0.85. \qquad (1)
\end{aligned}
$$

These criteria were defined to maximize completeness; one could alternatively choose to minimize contamination at the cost of increased incompleteness, but given the distribution of sources in Figure 2*b*, the differences would be small. This selection is only 7% incomplete for YSOs in our sample that have measured fluxes at 3.6 μm, 4.5 μm, and 8.0 μm, and has a contamination of less than 27% (the majority of the objects in this color box with uncertain classifications may still be YSOs). Approximately equivalent results can be obtained by substituting the [3.6]−[8.0] color for the [4.5]−[8.0] color, but it is slightly more difficult to avoid picking up stars on the blue end of the [3.6]−[8.0] color axis.

3.3.1. *Comparison to B07 Photometric Selection*

B07 identified a set of very bright YSOs across the entire SMC based on their 8.0 μm magnitudes and [5.8]−[8.0] colors. If we select the same region of the color-magnitude diagram in N66, we find 15 sources, only 3 of which are conclusively classified as YSOs. Almost all of the remaining objects have SEDs that are not well-fit by any of the models we apply, primarily because of PAH contamination. The PAH contamination across the rest of the galaxy should be much lower than in N66, so these numbers clearly represent a lower limit to the fraction of actual YSOs in the B07 sample.

3.4. *YSO Masses and Stages*

YSOs are traditionally divided into classes based on their observed spectral indices as originally defined by Lada (1987). Because spectral indices can vary with inclination angle as well as with evolutionary state, Robitaille et al. (2006) described their YSO models in terms of "stages", which are analogous to the usual classes, but are based on the physical quantities that define the evolutionary stage of the models. When comparing these models to data (rather than considering only observations), it therefore makes sense to use the stage system. The definitions of each stage rely on the ratio of the disk mass and envelope accretion rate to the central stellar mass. Stage I sources have $\dot{M}/M_* > 10^{-6}$, Stage II sources have $\dot{M}/M_* < 10^{-6}$ and $M_{disk}/M_* > 10^{-6}$, and Stage III sources have $\dot{M}/M_* < 10^{-6}$ and $M_{disk}/M_* < 10^{-6}$, where $\dot{M}$ is the envelope accretion rate. Note that we assumed a dust-to-gas ratio of 2×10^{-3} (1/5 of the Milky Way value) for N66 (Leroy et al. 2007).[12]

Using this classification scheme, we have grouped the 111 definite and probable YSOs in N66 into stages. The SEDs of most objects can be fit by more than 1 YSO model, so we first selected the models that produce a χ^2 that is within 1 of the best χ^2 for each object. We then computed a stage for each of the acceptable models and calculated a weighted average stage, using the χ^2 values as weights. The averages were rounded to the nearest integer to produce a classification. We find that of the

[12] The dust-to-gas ratio does not affect the YSO fits themselves, but does change the mass ratios between the disk and the central star, which is used for the stage classification.

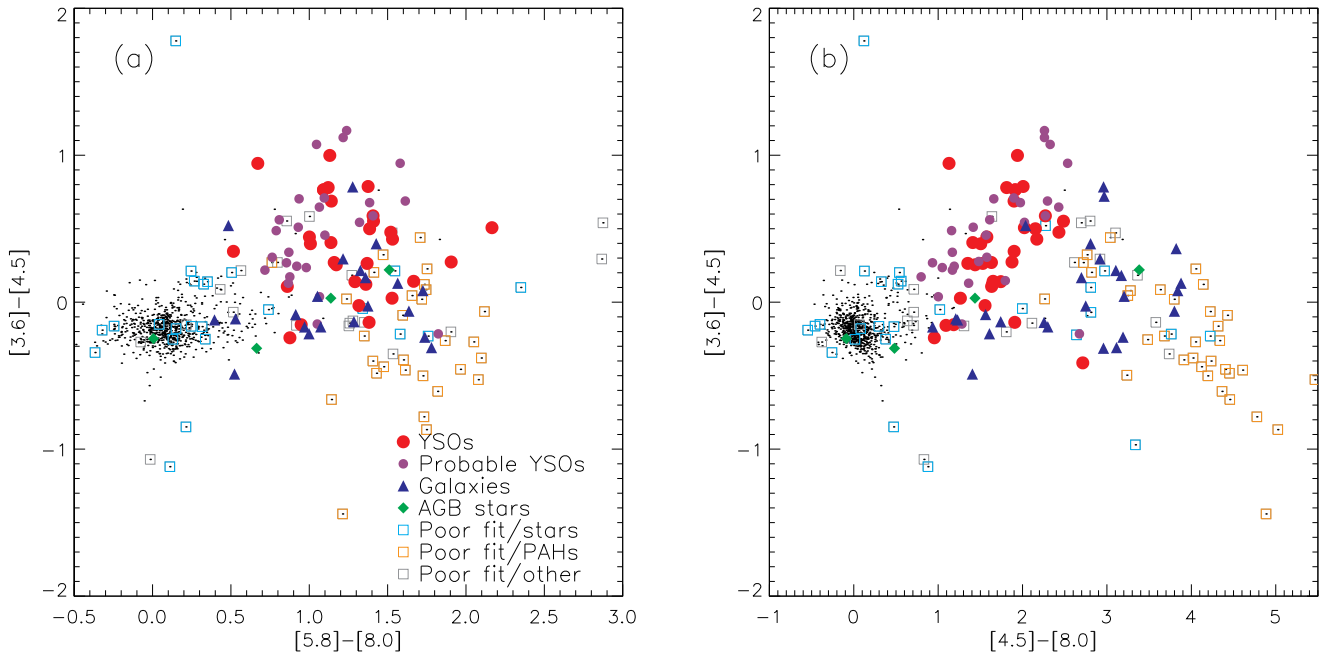

FIG. 2.— (*a*) IRAC [3.6]−[4.5] vs. [5.8]−[8.0] color-color diagram of N66. The black dots represent all detected sources (primarily stars), the filled red circles represent objects that can only be fit by YSO models, the smaller purple circles represent objects that are best fit by YSO models, although galaxy and/or AGB fits with significantly higher χ^2 values are also acceptable, the filled blue triangles are background galaxies, and the filled green diamonds are AGB stars. The open squares represent sources for which satisfactory fits were not obtained: the cyan symbols have SEDs that suggest they are likely to be stars, the orange symbols are sources that are contaminated by PAH emission features, and the gray symbols are the remaining unclassified poor fits. Note that the separation of YSOs from the other classes of sources is not very clean in this diagram. (*b*) IRAC [3.6]−[4.5] vs. [4.5]−[8.0] color-color diagram of N66. Symbols are the same as in (*a*). This plot offers the best separation of YSOs from the various contaminants, although there are still a few extragalactic sources that have similar colors to the YSOs.

111 YSOs, 33 are Stage I, 50 are Stage II, and 28 are Stage III.

We also calculated YSO masses with the same weighted averaging scheme, and defined the uncertainty on the mass to be the weighted standard deviation of the masses of the acceptable models. We found YSOs with a range of masses from $2.4 - 16.6$ $M_\odot$, including 19 objects that appear to be proto-OB stars ($M \geq 8$ $M_\odot$). We list the names, positions, luminosities, luminosity uncertainties (ΔL, the weighted standard deviation of the luminosities of the acceptable models), masses, mass uncertainties (ΔM, as defined in the first sentence of this paragraph), stages, and stage uncertainties (ΔStage, the weighted standard deviation of the stages of the acceptable models) of all of the YSOs in Table 1.

3.5. *Spatial Distribution of YSO Candidates*

In Figure 3 we plot the spatial distribution of the YSOs in N66. The protostars are obviously highly concentrated towards the peaks of the 8.0 μm emission. However, there is also star formation taking place outside of the dense dust cloud that marks the optical H II region, particularly to the south and southeast. Massey et al. (1989) hypothesized that star formation in N66 has proceeded from the southwest to the center of the present-day H II region, but we do find a few probable YSOs southwest of N66, indicating that at least modest star formation has taken place there within the past few million years.

The distribution of YSOs throughout the H II region as a function of mass and stage is not uniform. We find that the most-embedded objects (Stage I) are slightly

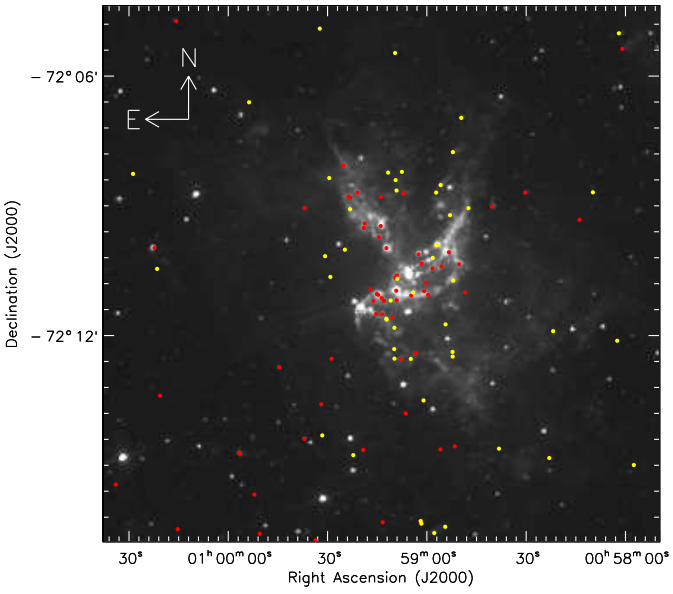

FIG. 3.— Spatial distribution of YSOs in N66, overplotted on an image of the 8.0 μm emission. The red circles represent objects with SEDs that can only be fit by YSO models, and the yellow circles represent objects that are probably YSOs but can be fit by other source types as well (albeit with significantly higher χ^2 values). The image is displayed on a logarithmic scale from 4 MJy sr^{-1} to 20 MJy sr^{-1}.

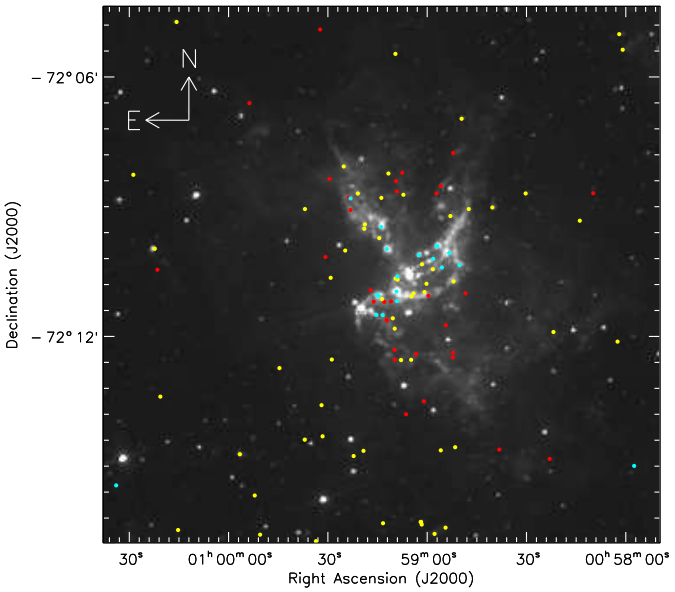

FIG. 4.— Mass distribution of YSOs in N66, overplotted on an image of the 8.0 μm emission. The most massive sources ($M >$ 8 $M_\odot$) are plotted as cyan points, and then decreasing masses are indicated by yellow (4.5 $M_\odot < M \leq$ 8 $M_\odot$) and red ($M \leq$ 4.5 $M_\odot$) points. The high-mass stars are more concentrated in the center of the H II region than the less massive objects. Note that the objects shown in this figure include the full YSO sample, not just the 61 definite YSOs that can only be fit by YSO SEDs.

more concentrated towards the center of the H II region than the more advanced (and presumably older) YSOs. We also see evidence for mass segregation, with the most massive objects exhibiting a strong preference for locations close to the center (see Figure 4). All but 2 of the YSOs with $M \geq 8$ $M_\odot$ lie on top of bright dust filaments in the main H II region, and many of them are coincident with molecular peaks and optical star clusters (Rubio et al. 2000; Sabbi et al. 2007). If these massive YSOs are indeed single objects rather than multiple unresolved sources, then the mass segregation must be primordial in origin, as the YSOs have not had time to move very far from their birthplaces.

4. DISCUSSION

The census of previously known embedded protostars in the SMC consists of a single object discovered by Gatley et al. (1982). Beaulieu et al. (2001) and de Wit et al. (2003) used variability data and Hα imaging to uncover a small sample of Herbig Ae/Be stars in the SMC, and Nota et al. (2006) discovered several hundred low-mass pre-main-sequence stars in N66 via isochrone fits to *HST* photometry. These objects, however, are generally much more evolved than the YSOs identified by this study, many of which are still embedded in their natal dust clouds and are therefore faint or invisible at optical wavelengths. The distribution of YSOs is concentrated towards clumps of molecular gas traced by the CO(2-1) emission line (Rubio et al. 2000) and the peaks of the dust emission at 7 μm (Contursi et al. 2000). Rubio et al. (2000) showed that dense H_2 knots are associated with these molecular clumps and suggested that massive star formation could be taking place there. The large number of embedded YSOs found in this study confirms that prediction. Moreover, IR spectroscopy of the 3 brightest embedded sources detected with ground-based near-IR imaging confirm that these sources are YSOs (Rubio and Barbá, in preparation).

The sample of Stage I, II, and III YSOs that we have identified in N66 presents the first opportunity for studying in detail a large sample of embedded YSOs in another galaxy (see also Jones et al. 2005; Chu et al. 2005), and more importantly, one whose ISM properties differ substantially from those of the Milky Way. The fact that we are able to identify over 100 YSOs in N66, as well as obtain successful SED fits for almost all of the other sources, suggests (perhaps surprisingly) that protostars in the SMC resemble the YSO models constructed by Whitney et al. for Milky Way objects, even though the metallicity and dust-to-gas ratio are a factor of ~ 5 lower in the SMC. The only potential difference between Milky Way and SMC YSOs that is evident in our results is that some of the sources are best fit by relatively cool photospheres, but the YSO models with such photospheres do not have high enough luminosities to match their observed brightnesses at the distance of the SMC. If these objects are actually YSOs, this problem could be an indication that accretion is continuing even after these stars have reached the main sequence, which leads to expanded photospheres and lower temperatures compared to normal pre-main sequence tracks and zero-age main-sequence photospheres (McKee & Tan 2003). An alternative possibility is that these sources actually consist of multiple cool protostars, which would explain their unusually high luminosities. The luminosities of these objects are $2-3$ orders of magnitude higher than the expected luminosities of individual YSOs of the same temperature, however, which makes the multiplicity explanation appear unlikely. Finally, evolved stars in the post-AGB phase also have expanded cool photospheres, so it is possible that some of the "cool luminous" sources could be post-AGB stars. Additional modeling and observations of some representative objects may be necessary to resolve this issue.

4.1. *The Star Formation Rate in N66*

The 111 YSOs in our sample have a combined stellar mass of 692 $M_\odot$. The observed mass function (see Figure 5) turns over at ~ 4 $M_\odot$, indicating that incompleteness becomes serious at this point. Artificial star tests in our photometry show that we are 90% complete even in the confused central region of N66 down to flux levels of 300 μJy, 200μJy, 200μJy, and 300 μJy from 3.6-8.0 μm. Applying these limits to the full library of YSO models confirms that our incompleteness is severe below 4 $M_\odot$. If we assume that star formation in N66 follows a Salpeter (1955) initial mass function (IMF) down to 0.1 $M_\odot$, we calculate that the total mass in protostars for the entire H II region is ~ 3160 $M_\odot$. In reality, this is a lower limit to the mass because even at 4 $M_\odot$ the data are somewhat incomplete. If these YSOs have all formed within the last ~ 1 Myr, then the average star formation rate over that time is 3.2×10^{-3} $M_\odot$ yr^{-1}. Thus, we find that N66 comprises at least $\sim 6\%$ of the total current star formation in the SMC.

4.2. *Comparison with Optical Observations*

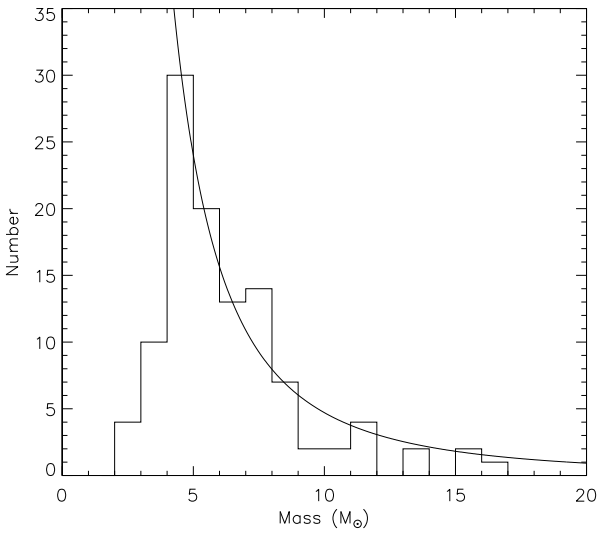

FIG. 5.— Mass function of YSOs in N66. The solid curve shows the best-fitting Salpeter IMF, which provides a reasonable fit to the data above 4 $M_\odot$, where the observational incompleteness becomes severe.

Nota et al. (2006), Gouliermis et al. (2006), and Sabbi et al. (2007) used *HST* imaging to study the young stellar population of N66 in the optical. Sabbi et al. (2007) identified 16 subclusters of pre-main sequence stars (their Figure 8; several of these clusters were also pointed out by Gouliermis et al.) in the H II region, and we find that all but two of these also have YSOs associated with them (see below). Sabbi et al. estimated ages of $\sim$ 3 Myr for the first 15 of the subclusters, but our detection of YSOs demonstrates that star formation has continued until the present day in these areas.

Subcluster 1 (Sc 1) is nearly coincident with an extremely bright *Spitzer* source (the 4th-most luminous object in the field at 8.0 μm), SSTS3MC 14.7725-72.1766, which we are able to fit with both YSO and AGB SEDs with similar χ^2 values. Given the location of this object at the center of the NGC 346 cluster, surrounded by numerous very young massive stars, it is most likely a YSO (nevertheless, since it does not formally meet our selection criteria it is not included in our analysis). If so, the fitted SEDs suggest that this is a Stage I object with a luminosity of 3.3×10^4 $L_\odot$ and a mass of 14.7 $M_\odot$. However, it is important to remember that because of the very high source density here we may actually be seeing multiple unresolved YSOs. In that case, we would be likely to overestimate the mass of the most massive YSO and underestimate the total mass of YSOs contained in this source. This type of source confusion should not have a strong effect on the SED fitting results, because the observed SED will be dominated by that of the most massive embedded YSO. A mid-IR spectrum of this object is displayed in Contursi et al. (2000, peak C). Another bright *Spitzer* source, SSTS3MC 14.7748-72.1749, is located within 3″ of Sc 1 and has a steeply-rising mid- and far-IR SED that we are unable to fit successfully. If we remove the 24 μm upper limit and either the 70 μm or J- and K-band detections (perhaps justified because of confusion in this very densely populated region), then this source has the SED of a very massive ($M > 10$ $M_\odot$), early-stage YSO. We do not detect any non-stellar sources in Sc 3 (immediately south of Sc 1), but confusion as a result of the very bright source just north of the cluster may play a role in this non-detection.

Sc 2 is located very close to 2 *Spitzer* sources. SSTS3MC 14.7574 has a stellar SED with a strong 24 μm detection (indicating either confusion or circumstellar dust) and SSTS3MC 14.7580-72.1763 is formally a poor fit as a result of a low K-band flux and slight PAH contamination, but appears to have an SED consistent with being an early stage YSO.

Scs 4-6 each have bright infrared counterparts. Sc 4 is coincident with SSTS3MC 14.7605-72.1687, a massive embedded YSO. Sc 5 is SSTS3MC 14.7514-72.1681, another object that can be fitted by both YSO and AGB SEDs. Again, given its position in a very young cluster, it is most likely a massive stage I YSO rather than an evolved star. And Sc 6 contains 2 blended *Spitzer* sources, SSTS3MC 14.7371-72.1651 and SSTS3MC 14.7380-72.1651, both very high-mass stage I YSOs. The caveat mentioned above about multiple unresolved sources applies here as well.

Located on the southern edge of Sc 7, very close to the prominent dust lane that arcs nearly halfway around N66, is SSTS3MC 14.7733-72.1835, yet another very massive (18.6 $M_\odot$) stage I protostar that can also be fit by AGB models. Slightly further to the southwest are 2 additional, lower-mass YSOs, SSTS3MC 14.7673-72.1834 and SSTS3MC 14.7698-72.1846.

Sc 8 has a faint *Spitzer* counterpart, SSTS3MC 14.7816-72.1802, which shows a stellar SED in the optical and near-IR and excesses in the IRAC bands, but is not fit well by any of our YSO models. It is possible that the optical and IR emission is coming from different sources.

Scs 9-11 are located around a quintet of YSOs. The 2 brightest of these, SSTS3MC 14.8112-72.1843 and SSTS3MC 14.8130-72.1840, lie within Sc 10, but it is not clear whether these are truly blended YSOs as opposed to a bright, extended clump of dust. The other 3 sources classified as YSOs in this region are SSTS3MC 14.8041-72.1867, SSTS3MC 14.8068-72.1856, and SSTS3MC 14.8174-72.1866.

Sc 12 contains two bright *Spitzer* sources (SSTS3MC 14.8318-72.1890 and SSTS3MC 14.8353-72.1892) that are not fit well by any of the available models. The rising SEDs of these objects towards long wavelengths strongly suggest that there are YSOs present here, but blending may be a problem. This cluster is coincident with the source labeled peak I by Contursi et al. (2000).

Scs 13-15 lie in the northward extension of the H II region (N66A). Clusters 13 and 14 each overlap with a YSO (SSTS3MC 14.8009-72.1663 = Contursi et al. peak F and SSTS3MC 14.8080-72.1578 = Contursi et al. peak G), but as with Sc 10 the source in Sc 14 does not appear pointlike in the IRAC bands, and so may not be a single object. Sc 15 is associated with SSTS3MC 14.8205-72.1544, which shows very strong PAH emission but is not well-fit by YSO models.

Finally, Sc 16 contains 2 *Spitzer* sources, but both of these are well-fit by normal stellar models, consistent with the older age of this cluster derived by Sabbi et al. (2007).

Out of the 44 YSOs in our sample that lie within the ACS Hα images of Nota et al. (2006), $\sim$ 10 are spatially coincident with gas or dust pillars strongly resembling those made famous by *HST* imaging of the "Pillars of Creation" in the Eagle Nebula (Hester et al. 1996). Higher spatial resolution near-IR and mid-IR imaging of these objects may reveal exactly how the YSOs are related to these features.

5. SUMMARY AND CONCLUSIONS

We have obtained mid-infrared imaging of the H II region N66 (NGC 346) in the SMC with the IRAC and MIPS instruments on the *Spitzer Space Telescope*. We detected 8011 unique sources, with photometric coverage extending from V-band to 24 μm (70 μm in a few cases). Most of these sources have colors and SEDs consistent with being normal stars, but we also detect a significant population of objects that are very red in the mid-IR. SED fitting of the 1645 sources with photometric measurements in at least four bands yielded 111 objects with SEDs that are best fit by YSO models rather than stars or background galaxies. These data represent the first significant sample of embedded YSOs identified in an external galaxy.

We show that these YSOs can be mostly, but not completely, separated from stars on the basis of their IRAC colors. However, SED fitting is necessary to significantly constrain the properties of individual objects. We find that the YSO models of Whitney et al. (2003a,b, 2004), which were designed to represent Milky Way YSOs with solar metallicities, fit most of the YSOs in N66 well, despite its much lower metallicity and dust-to-gas ratio. These results suggest that if low metallicity causes significant changes in the star formation process, the threshold for those effects must lie below the metallicity of the SMC ($12 + \log[\mathrm{O/H}] \approx 8.0$; Dufour 1975). The one possible difference between SMC and Milky Way YSOs is that the SMC appears to contain a population of very luminous but cool objects that have not been seen in the Milky Way. These objects may have expanded photospheres and hence lower temperatures than normal because they are still accreting material from their protostellar disks when they reach the main sequence. Alternatively, these sources could be multiple cool YSOs that are unresolved by *Spitzer*.

We calculate masses and stages (analogous to the usual YSO classes) for each of the N66 YSOs, finding a range of masses from 2.4 to 16.6 $M_\odot$ (including 19 objects with masses above 8 $M_\odot$). Almost half (45%) of the YSOs are Stage II objects, 30% are Stage I, and the remaining 25% are evolved Stage III sources. We examine the spatial distribution of the YSOs and find that they are strongly concentrated in the center of the H II region where bright Hα and dust emission is seen, but there are also small numbers of YSOs in the surrounding region with much less diffuse ISM emission. The most massive YSOs are preferentially located closer to the center of N66, indicating that mass segregation is taking place. We compare our YSO map to the clusters of pre-main sequence stars identified in the optical by Sabbi et al. (2007) and find that all but 2 of the clusters have associated YSOs. Using a Salpeter IMF, we calculate that a total of at least 3160 $M_\odot$ of YSOs have been formed in the last $\sim 10^6$ yr, representing $\gtrsim 6\%$ of the current star formation in the SMC.

We would like to thank the anonymous referee for a careful reading of the paper that produced valuable feedback. J.D.S. gratefully acknowledges the support of a Millikan Fellowship provided by the California Institute of Technology. This research was partially funded by NASA through an award issued by JPL/Caltech (NASA-JPL *Spitzer* grant 1264151 awarded to Cycle 1 project 3316). B.W. was supported by NASA Astrophysics Theory Program grant NNG05GH35G and the *Spitzer* Theoretical Research Program under Subcontract 1290701, M.R. was supported by the Chilean *Center for Astrophysics* FONDAP No. 15010003, and financial support from FONDECYT No. 1050052 is acknowledged by R.H.B. We thank You-Hua Chu, Robert Gruendl, Lynne Hillenbrand, Jacco van Loon, Adam Leroy, and Bob Benjamin for helpful conversations, and we also thank Dimitrios Gouliermis for providing us with the *HST* photometry in advance of publication. This work is based on observations made with the *Spitzer Space Telescope*, which is operated by the Jet Propulsion Laboratory, California Institute of Technology under a contract with NASA. This publication makes use of data products from the Two Micron All Sky Survey, which is a joint project of the University of Massachusetts and the Infrared Processing and Analysis Center/California Institute of Technology, funded by NASA and the National Science Foundation. This research has also made use of NASA's Astrophysics Data System Bibliographic Services and the SIMBAD database, operated at CDS, Strasbourg, France.

REFERENCES

Allen, L. E., et al. 2004, ApJS, 154, 363
Beaulieu, J.-P., et al. 2001, A&A, 380, 168
Bolatto, A. D., et al. 2007, ApJ, 655, 212 (B07)
Brott, I., & Hauschildt, P. H. 2005, ESA SP-576: The Three-Dimensional Universe with Gaia, 565
Cartledge, S. I. B., et al. 2005, ApJ, 630, 355
Chu, Y.-H., et al. 2005, ApJ, 634, L189
Contursi, A., et al. 2000, A&A, 362, 310
Dale, D. A., et al. 2005, ApJ, 633, 857
de Vaucouleurs, G., de Vaucouleurs, A., Corwin, H. G., Buta, R. J., Paturel, G., & Fouqué, P. 1991, Third Reference Catalog of Bright Galaxies (Berlin: Springer-Verlag)
de Wit, W. J., Beaulieu, J.-P., Lamers, H. J. G. L. M., Lesquoy, E., & Marquette, J.-B. 2003, A&A, 410, 199
Dufour, R. J. 1975, ApJ, 195, 315
Dufour, R. J., & Harlow, W. V. 1977, ApJ, 216, 706
Fazio, G. G., et al. 2004, ApJS, 154, 10
Fujii, T., & Nakada, Y. 2003, Astrophysics and Space Science Library, 283, 221
Gatley, I., Hyland, A. R., & Jones, T. J. 1982, MNRAS, 200, 521
Gordon, K. D., Clayton, G. C., Misselt, K. A., Landolt, A. U., & Wolff, M. J. 2003, ApJ, 594, 279
Gouliermis, D. A., Dolphin, A. E., Brandner, W., & Henning, T. 2006, ApJS, 166, 549
Henize, K. G. 1956, ApJS, 2, 315
Hester, J. J., et al. 1996, AJ, 111, 2349
Hilditch, R. W., Howarth, I. D., & Harries, T. J. 2005, MNRAS, 357, 304
Hony, S. 2002, Ph.D. Thesis, University of Amsterdam
Hony, S., Waters, L. B. F. M., & Tielens, A. G. G. M. 2002, A&A, 390, 533
Jones, T. J., Woodward, C. E., Boyer, M. L., Gehrz, R. D., & Polomski, E. 2005, ApJ, 620, 731
Keller, S. C., & Wood, P. R. 2006, ApJ, 642, 834

Kurucz, R. L. 1992, IAU Symp. 149: The Stellar Populations of Galaxies, 149, 225
Lada, C. J. 1987, IAU Symp. 115: Star Forming Regions, 115, 1
Leroy, A., Bolatto, A., Stanimirović, S., Mizuno, N., Israel, F., & Bot, C. 2007, ApJ, in press (preprint: astro-ph/0611687)
Makovoz, D., & Marleau, F. R. 2005, PASP, 117, 1113
Massey, P., Parker, J. W., & Garmany, C. D. 1989, AJ, 98, 1305
McKee, C. F., & Tan, J. C. 2003, ApJ, 585, 850
Molster, F. J., Waters, L. B. F. M., Tielens, A. G. G. M., & Barlow, M. J. 2002, A&A, 382, 184
Nota, A., et al. 2006, ApJ, 640, L29
Olivier, E. A., Whitelock, P., & Marang, F. 2001, MNRAS, 326, 490
Peimbert, M., Peimbert, A., & Ruiz, M. T. 2000, ApJ, 541, 688
Peimbert, M., & Torres-Peimbert, S. 1976, ApJ, 203, 581
Rieke, G. H., et al. 2004, ApJS, 154, 25
Robitaille, T. P., Whitney, B. A., Indebetouw, R., Wood, K., & Denzmore, P. 2006, ApJS, 167, 256
Robitaille, T. P., Whitney, B. A., Indebetouw, R., & Wood, K. 2007, ApJS, 169, 328
Rubio, M., Barbá, R., Boulanger, F., & Gallart, C. 2002, in ESO Workshop: The Origins of Stars and Planets: The VLT View (Berlin: Springer-Verlag)
Rubio, M., Contursi, A., Lequeux, J., Probst, R., Barbá, R., Boulanger, F., Cesarsky, D., & Maoli, R. 2000, A&A, 359, 1139
Sabbi, E., et al. 2007, AJ, 133, 44
Salpeter, E. E. 1955, ApJ, 121, 161
Silva, L., Granato, G. L., Bressan, A., & Danese, L. 1998, ApJ, 509, 103
Skrutskie, M. F., et al. 2006, AJ, 131, 1163
Stanimirović, S., Staveley-Smith, L., van der Hulst, J. M., Bontekoe, T. R., Kester, D. J. M., & Jones, P. A. 2000, MNRAS, 315, 791
Storm, J., Carney, B. W., Gieren, W. P., Fouqué, P., Latham, D. W., & Fry, A. M. 2004, A&A, 415, 531
Sylvester, R. J., Kemper, F., Barlow, M. J., de Jong, T., Waters, L. B. F. M., Tielens, A. G. G. M., & Omont, A. 1999, A&A, 352, 587
Westerlund, B. E. 1997, The Magellanic Clouds (Cambridge: Cambridge Univ. Press)
Whitney, B. A., Wood, K., Bjorkman, J. E., & Wolff, M. J. 2003, ApJ, 591, 1049
Whitney, B. A., Wood, K., Bjorkman, J. E., & Cohen, M. 2003, ApJ, 598, 1079
Whitney, B. A., Indebetouw, R., Bjorkman, J. E., & Wood, K. 2004, ApJ, 617, 1177
Wilke, K., Klaas, U., Lemke, D., Mattila, K., Stickel, M., & Haas, M. 2004, A&A, 414, 69

TABLE 1
YOUNG STELLAR OBJECTS IN N66

Number (1)	Source name (2)	α (J2000.0) (3)	δ (J2000.0) (4)	L ($L_\odot$) (5)	ΔL[a] ($L_\odot$) (6)	M_* ($M_\odot$) (7)	ΔM_*[a] ($M_\odot$) (8)	Stage (9)	ΔStage[a] (10)	χ^2 [b] (11)	χ^2_2 [c] (12)
				Definite YSOs							
1	SSTS3MC14.5039−72.0895	00 58 00.94	−72 05 22.3	1290	556	6.5	0.8	III	0.6	0.26	—
2	SSTS3MC14.5579−72.1554	00 58 13.89	−72 09 19.5	131	—	5.1	—	I	—	1.76	—
3	SSTS3MC14.6261−72.1449	00 58 30.26	−72 08 41.5	328	107	4.6	0.4	II	0.4	0.12	—
4	SSTS3MC14.6680−72.1503	00 58 40.31	−72 09 01.0	1590	1600	6.0	2.5	II	0.5	0.40	—
5	SSTS3MC14.7018−72.1834	00 58 48.43	−72 11 00.2	35	2	2.8	0.5	I	—	4.06	—
6	SSTS3MC14.7094−72.1725	00 58 50.25	−72 10 20.9	3300	—	8.3	—	III	—	5.53	—
7	SSTS3MC14.7148−72.2427	00 58 51.55	−72 14 33.9	671	353	5.3	0.9	III	0.5	0.95	—
8	SSTS3MC14.7223−72.1679	00 58 53.35	−72 10 04.3	3520	789	8.9	1.5	I	—	1.39	—
9	SSTS3MC14.7315−72.1734	00 58 55.56	−72 10 24.3	4430	—	9.0	—	III	—	1.37	—
10	SSTS3MC14.7329−72.2439	00 58 55.90	−72 14 38.1	261	—	6.4	—	I	—	6.15	—
11	SSTS3MC14.7429−72.1741	00 58 58.30	−72 10 26.9	4340	—	7.9	—	I	—	3.55	—
12	SSTS3MC14.7485−72.1843	00 58 59.63	−72 11 03.3	348	—	4.5	—	II	—	1.68	—
13	SSTS3MC14.7509−72.1797	00 59 00.22	−72 10 47.0	1940	—	7.3	—	III	—	2.37	—
14	SSTS3MC14.7534−72.1829	00 59 00.81	−72 10 58.6	388	1	4.7	—	II	—	5.48	—
15	SSTS3MC14.7566−72.1722	00 59 01.58	−72 10 19.8	2230	—	7.5	—	II	—	0.68	—
16	SSTS3MC14.7582−72.2715	00 59 01.96	−72 16 17.5	306	813	4.6	1.1	II	0.7	0.41	—
17	SSTS3MC14.7605−72.1687	00 59 02.53	−72 10 07.4	5120	2210	10.3	0.8	I	0.4	3.69	—
18	SSTS3MC14.7639−72.2068	00 59 03.34	−72 12 24.3	197	46	3.9	0.2	II	—	0.56	—
19	SSTS3MC14.7698−72.1846	00 59 04.75	−72 11 04.7	684	7	5.5	—	II	—	0.50	—
20	SSTS3MC14.7766−72.2300	00 59 06.37	−72 13 48.0	369	214	4.5	0.7	II	0.5	0.00	—
21	SSTS3MC14.7800−72.1454	00 59 07.19	−72 08 43.4	261	—	6.4	—	I	—	9.19	—
22	SSTS3MC14.7829−72.2091	00 59 07.90	−72 12 32.9	459	151	4.9	0.4	II	—	6.59	—
23	SSTS3MC14.7876−72.1769	00 59 09.03	−72 10 37.0	4430	—	9.0	—	III	—	1.44	—
24	SSTS3MC14.7880−72.1864	00 59 09.13	−72 11 11.0	9880	—	11.6	—	III	—	13.16	—
25	SSTS3MC14.7886−72.1827	00 59 09.25	−72 10 57.8	30300	—	16.6	—	I	—	6.79	—
26	SSTS3MC14.7898−72.1777	00 59 09.55	−72 10 39.6	1620	—	7.0	—	III	—	3.99	—
27	SSTS3MC14.7933−72.1930	00 59 10.40	−72 11 34.9	6540	12500	7.9	8.3	I	—	12.36	—
28	SSTS3MC14.8009−72.1663	00 59 12.22	−72 09 58.8	5060	—	10.1	—	I	—	9.19	—
29	SSTS3MC14.8041−72.1867	00 59 12.98	−72 11 12.3	176	15	3.8	—	II	—	0.81	—
30	SSTS3MC14.8056−72.2720	00 59 13.33	−72 16 19.1	456	245	4.8	0.7	III	0.5	0.01	—
31	SSTS3MC14.8061−72.1918	00 59 13.46	−72 11 30.5	5990	2100	13.1	3.1	I	—	6.52	—
32	SSTS3MC14.8068−72.1856	00 59 13.62	−72 11 08.0	540	131	5.2	0.4	II	—	0.18	—
33	SSTS3MC14.8077−72.1466	00 59 13.85	−72 08 47.7	728	159	5.6	0.3	III	—	5.52	—
34	SSTS3MC14.8080−72.1578	00 59 13.92	−72 09 27.9	8380	1470	11.0	0.6	II	0.7	8.32	—
35	SSTS3MC14.8104−72.1621	00 59 14.49	−72 09 43.7	387	—	4.7	—	II	—	7.82	—
36	SSTS3MC14.8112−72.1843	00 59 14.68	−72 11 03.4	13000	7940	15.1	2.9	I	—	1.17	—
37	SSTS3MC14.8130−72.1840	00 59 15.11	−72 11 02.2	9560	2180	11.4	0.8	II	0.5	5.23	—
38	SSTS3MC14.8140−72.1917	00 59 15.36	−72 11 30.0	3300	—	8.3	—	III	—	0.42	—
39	SSTS3MC14.8174−72.1866	00 59 16.18	−72 11 11.6	210	61	4.0	0.2	II	—	1.00	—
40	SSTS3MC14.8211−72.1822	00 59 17.07	−72 10 55.8	87	10	4.5	0.3	I	—	6.43	—
41	SSTS3MC14.8284−72.1568	00 59 18.82	−72 09 24.3	1180	—	6.4	—	II	—	4.08	—
42	SSTS3MC14.8292−72.1585	00 59 19.00	−72 09 30.5	656	—	5.5	—	II	—	4.88	—
43	SSTS3MC14.8302−72.2441	00 59 19.25	−72 14 38.8	453	174	4.9	0.8	III	0.5	0.00	—
44	SSTS3MC14.8373−72.1449	00 59 20.95	−72 08 41.5	922	345	6.2	0.4	II	0.3	0.15	—
45	SSTS3MC14.8465−72.1468	00 59 23.16	−72 08 48.4	4430	1780	8.8	1.7	III	0.3	2.67	—
46	SSTS3MC14.8487−72.1464	00 59 23.69	−72 08 47.1	204	60	3.9	0.3	II	—	2.78	—
47	SSTS3MC14.8551−72.1345	00 59 25.22	−72 08 04.1	1340	—	6.6	—	III	—	0.40	—
48	SSTS3MC14.8701−72.2089	00 59 28.83	−72 12 31.9	131	—	5.1	—	I	—	6.78	—
49	SSTS3MC14.8830−72.2265	00 59 31.91	−72 13 35.3	206	—	5.9	—	I	—	5.28	—
50	SSTS3MC14.8900−72.2789	00 59 33.61	−72 16 43.9	678	215	5.5	0.5	III	—	2.11	—
51	SSTS3MC14.9039−72.1509	00 59 36.94	−72 09 03.2	77	11	4.6	0.3	I	0.4	3.33	—

TABLE 1 — *Continued*

Number (1)	Source name (2)	α (J2000.0) (3)	δ (J2000.0) (4)	L ($L_\odot$) (5)	ΔL[a] ($L_\odot$) (6)	M_* ($M_\odot$) (7)	ΔM_*[a] ($M_\odot$) (8)	Stage (9)	ΔStage[a] (10)	χ^2 [b] (11)	χ^2_2 [c] (12)
52	SSTS3MC14.9041−72.2398	00 59 36.98	−72 14 23.2	1000	495	5.8	1.5	II	0.2	0.22	—
53	SSTS3MC14.9360−72.2122	00 59 44.64	−72 12 44.0	2150	—	7.5	—	III	—	7.94	—
54	SSTS3MC14.9603−72.2764	00 59 50.48	−72 16 35.2	644	249	5.4	0.6	III	0.5	0.51	—
55	SSTS3MC14.9671−72.2613	00 59 52.12	−72 15 40.8	529	376	5.0	0.9	II	0.5	0.21	—
56	SSTS3MC14.9858−72.2454	00 59 56.59	−72 14 43.5	683	177	5.9	0.8	II	0.4	11.79	—
57	SSTS3MC15.0636−72.2746	01 00 15.27	−72 16 28.7	1000	—	6.2	—	III	—	5.99	—
58	SSTS3MC15.0655−72.0788	01 00 15.72	−72 04 43.6	360	87	4.6	0.4	II	—	0.26	—
59	SSTS3MC15.0859−72.2232	01 00 20.62	−72 13 23.6	488	119	5.0	0.3	II	0.5	7.91	—
60	SSTS3MC15.0930−72.1662	01 00 22.32	−72 09 58.2	2910	944	8.0	0.7	I	0.5	0.40	—
61	SSTS3MC15.1415−72.2574	01 00 33.97	−72 15 26.5	1750	99	8.8	0.4	I	—	5.55	—
				Probable YSOs							
62	SSTS3MC14.4895−72.2499	00 57 57.49	−72 14 59.7	12700	10900	11.4	5.3	III	—	1.95	3.49
63	SSTS3MC14.5083−72.0835	00 58 02.00	−72 05 00.7	2000	2130	7.0	2.3	II	0.4	0.04	8.60
64	SSTS3MC14.5104−72.2020	00 58 02.50	−72 12 07.0	573	536	5.1	1.5	II	0.8	0.02	4.23
65	SSTS3MC14.5410−72.1448	00 58 09.85	−72 08 41.2	160	107	4.0	0.8	II	0.5	0.28	1.45
66	SSTS3MC14.5911−72.1983	00 58 21.87	−72 11 53.8	114	—	5.0	—	I	—	5.85	10.50
67	SSTS3MC14.5959−72.2472	00 58 23.01	−72 14 50.0	95	93	4.3	0.9	I	0.4	0.60	7.06
68	SSTS3MC14.6593−72.2436	00 58 38.23	−72 14 37.0	210	300	3.7	1.1	II	0.5	0.01	2.29
69	SSTS3MC14.6977−72.1509	00 58 47.45	−72 09 03.2	2290	188	7.6	0.2	III	—	5.99	14.70
70	SSTS3MC14.7067−72.1161	00 58 49.60	−72 06 58.0	1470	2230	6.5	1.2	II	0.3	0.05	3.93
71	SSTS3MC14.7169−72.1788	00 58 52.04	−72 10 43.8	517	900	4.8	0.9	II	0.2	2.20	7.18
72	SSTS3MC14.7173−72.1293	00 58 52.16	−72 07 45.4	260	317	4.3	0.6	II	0.2	0.07	1.78
73	SSTS3MC14.7175−72.2081	00 58 52.19	−72 12 29.1	80	16	4.1	1.0	I	—	4.49	12.55
74	SSTS3MC14.7177−72.2063	00 58 52.24	−72 12 22.6	37	69	2.9	0.8	II	0.6	0.00	0.32
75	SSTS3MC14.7208−72.1536	00 58 53.00	−72 09 12.9	1640	307	7.0	0.4	III	—	0.06	1.01
76	SSTS3MC14.7265−72.1957	00 58 54.36	−72 11 44.6	59	105	2.4	4.6	I	—	0.01	2.38
77	SSTS3MC14.7269−72.2737	00 58 54.45	−72 16 25.1	1170	861	6.4	2.3	III	0.5	0.00	2.29
78	SSTS3MC14.7327−72.1420	00 58 55.85	−72 08 31.3	236	—	4.0	—	I	—	3.05	11.44
79	SSTS3MC14.7371−72.1651	00 58 56.89	−72 09 54.5	9390	3200	13.5	1.8	I	—	3.54	10.49
80	SSTS3MC14.7380−72.1651	00 58 57.11	−72 09 54.3	14800	7190	15.5	2.4	I	—	0.18	1.96
81	SSTS3MC14.7383−72.1449	00 58 57.19	−72 08 41.5	231	370	4.1	1.0	II	0.5	0.02	1.76
82	SSTS3MC14.7407−72.2761	00 58 57.76	−72 16 34.0	1210	874	6.4	0.6	II	0.6	0.48	1.57
83	SSTS3MC14.7426−72.1701	00 58 58.23	−72 10 12.4	3290	—	8.3	—	III	—	0.32	1.64
84	SSTS3MC14.7542−72.2250	00 59 01.01	−72 13 30.1	257	469	4.2	0.8	II	0.4	0.00	3.06
85	SSTS3MC14.7569−72.2725	00 59 01.65	−72 16 21.1	251	—	6.5	—	I	—	2.77	8.52
86	SSTS3MC14.7577−72.2715	00 59 01.86	−72 16 17.4	726	1020	5.2	1.4	II	0.6	0.00	6.20
87	SSTS3MC14.7673−72.1834	00 59 04.14	−72 11 00.1	2290	1870	7.0	1.9	II	0.7	2.42	8.66
88	SSTS3MC14.7702−72.2090	00 59 04.84	−72 12 32.5	310	47	6.7	0.5	I	—	0.96	3.43
89	SSTS3MC14.7814−72.1369	00 59 07.54	−72 08 12.8	176	151	3.6	0.7	III	0.5	0.50	2.90
90	SSTS3MC14.7872−72.1781	00 59 08.93	−72 10 41.2	2360	—	7.6	—	II	—	0.20	6.33
91	SSTS3MC14.7882−72.1441	00 59 09.17	−72 08 38.7	201	914	3.9	1.2	II	0.5	0.12	1.09
92	SSTS3MC14.7893−72.1401	00 59 09.43	−72 08 24.2	80	40	3.6	0.5	II	0.5	0.10	7.14
93	SSTS3MC14.7900−72.0911	00 59 09.60	−72 05 27.9	821	226	5.8	0.4	III	0.7	0.48	3.25
94	SSTS3MC14.7908−72.2089	00 59 09.80	−72 12 31.9	57	23	2.7	0.2	II	—	0.38	8.03
95	SSTS3MC14.7909−72.1970	00 59 09.81	−72 11 49.1	2270	1610	7.2	1.7	III	0.5	0.49	9.59
96	SSTS3MC14.7911−72.2052	00 59 09.87	−72 12 18.8	162	74	3.7	0.3	II	0.3	0.05	6.49
97	SSTS3MC14.7956−72.1865	00 59 10.93	−72 11 11.5	114	373	3.2	1.5	II	—	0.01	3.12
98	SSTS3MC14.7988−72.1372	00 59 11.72	−72 08 13.7	114	—	5.0	—	I	—	6.32	12.05
99	SSTS3MC14.8006−72.1939	00 59 12.13	−72 11 38.1	171	54	4.1	0.7	I	0.5	1.69	8.27
100	SSTS3MC14.8011−72.1935	00 59 12.25	−72 11 36.7	305	228	4.2	0.8	II	—	0.07	7.34
101	SSTS3MC14.8426−72.2461	00 59 22.23	−72 14 45.8	275	170	4.7	0.6	II	0.2	0.00	0.12
102	SSTS3MC14.8466−72.1513	00 59 23.19	−72 09 04.5	356	109	4.5	0.6	II	—	2.22	6.76
103	SSTS3MC14.8532−72.1669	00 59 24.77	−72 10 00.8	1160	90	7.0	0.7	II	1.0	0.70	7.04

TABLE 1 — *Continued*

Number (1)	Source name (2)	α (J2000.0) (3)	δ (J2000.0) (4)	L ($L_\odot$) (5)	ΔL[a] ($L_\odot$) (6)	M_* ($M_\odot$) (7)	ΔM_*[a] ($M_\odot$) (8)	Stage (9)	ΔStage[a] (10)	χ^2 [b] (11)	χ^2_2 [c] (12)
104	SSTS3MC14.8715−72.1774	00 59 29.15	−72 10 38.6	490	58	7.3	0.3	I	—	2.46	5.53
105	SSTS3MC14.8729−72.1393	00 59 29.49	−72 08 21.6	123	45	4.4	0.8	I	—	2.10	4.92
106	SSTS3MC14.8781−72.1694	00 59 30.74	−72 10 09.9	441	385	4.4	1.5	III	0.5	0.97	9.78
107	SSTS3MC14.8817−72.2385	00 59 31.60	−72 14 18.6	540	963	4.6	1.6	II	0.7	0.16	6.91
108	SSTS3MC14.8848−72.0817	00 59 32.35	−72 04 54.2	98	47	4.2	1.1	I	—	1.85	6.99
109	SSTS3MC14.9738−72.1101	00 59 53.70	−72 06 36.3	201	215	4.3	0.7	II	0.6	0.05	4.07
110	SSTS3MC15.0896−72.1743	01 00 21.49	−72 10 27.5	80	30	3.9	0.9	I	0.5	0.14	3.10
111	SSTS3MC15.1199−72.1377	01 00 28.78	−72 08 15.6	847	166	5.9	0.3	III	—	0.06	6.27

NOTE. — The coordinates in this table are not necessarily identical to the ones presented by B07 and made available on the S^{3}MC website because the N66 photometry was carried out independently. However, the differences should be very small.

[a] The uncertainties on the luminosities, masses, and stages are calculated as the weighted standard deviation of the luminosities, masses, and stages of all of the acceptable YSO models. In cases where there is only one acceptable model for a given source, or there are multiple models but they all produce the same luminosity/mass/stage, we cannot calculate an uncertainty in this way, so we leave the corresponding space in the table blank.[b] χ^2 value for the best fitting SED. Note that these are raw χ^2 values, not χ^2 per data point, so a good fit (χ^2 per data point ≤ 2.2) can have a χ^2 as high as 8.8 (if there are 4 flux data points for that source) or more.[c] χ^2 value for the best fitting AGB star or background galaxy SED.

TABLE 2
SED Classification Results

Object Class	Number
All sources	1645
Objects with unique SED classifications	
Normal stars	1322
YSOs	61
Galaxies	27
AGB stars	6
Objects without unique SED classifications	
Probable YSOs	50
Probable galaxies	13
Probable AGB stars	5
Multiple good fits; unable to classify	13
Poor fits	148